POLITECNICO
MILANO 1863

SCUOLA DI INGEGNERIA INDUSTRIALE
E DELL'INFORMAZIONE

Executive Summary of the Thesis

ANNs for 2D positioning and improved time resolution in monolithic TOF-PET detectors

Laurea Magistrale in Biomedical Engineering - Ingegneria Biomedica

Author: Riccardo Pallone

Advisor: Prof. Carlo Ettore Fiorini

Co-advisor: Ilenia D'Adda

Academic year: 2021-2022

1. Introduction

Monolithic detectors for PET and TOF-PET imaging systems are gaining more and more interest due to their higher sensitivity, timing resolution, and spatial resolution. Moreover, the spatial propagation of the scintillation light can be exploited to gain additional information on the temporal dynamics of the detection. This current thesis work aims to provide a complete data processing algorithm that provides predictions on 2D gamma-interaction positioning and improves the detector time resolution. Two artificial neural networks (ANNs) are implemented: a positioning ANN predicts the scintillation position, and a timing ANN predicts a correction for time of flight (TOF) measurements. The geometry of the detector under consideration consists of a monolithic crystal of dimensions 50.8x50.8x20 mm^3 coupled to an 8x8 matrix of SiPMs. The simulation toolkit ANTS2 is used to collect data from different detector configurations, using $LaBr_3$(Ce) and LYSO(Ce) crystals together with different coatings. The study includes comparisons between different spatially-resolved training datasets, collected by moving a pencil beam source with 1 mm and 5 mm step sizes. Both positioning and timing data are analyzed to evaluate the best data preparation. The positioning ANN showed a 1.805 mm spatial FWHM on a LYSO(Ce) + ESR configuration. The correction predicted by the timing ANN was able to reduce the TOF uncertainty from the initial value of 467 ps FWHM to the corrected one of 192 ps FWHM for the $LaBr_3$(Ce) + Teflon setup.

Positron emission tomography (PET) is an indirect and quantitative functional medical imaging modality that measures an activity distribution of a positron-emitting isotope. An isotope decays by emitting a positron which annihilates with an electron to form two back-to-back gamma photons at 511 keV. Subsequently, two PET detectors register the two detected gamma photons as a coincidence event within a certain time window and assume that they originate from the same annihilation, placed somewhere along the line connecting the two PET detectors. This line is called the line of response (LOR). The location of the emission point along the LOR is given by the difference in detection times, or time of flight (TOF) difference, of the two annihilation photons. This is the principle underlying TOF-PET imaging systems. The accuracy of this measurement is obviously related to the time resolution of the scanner. It is typically measured as the full-width-half-maximum (FWHM) of the time distribution of a point source, and it is usually reported as *coincidence rime resolution* (CTR). Even if an exact time measurement is still not possible, higher TOF resolutions allow more precise localization of the event along the LOR, which leads to an higher signal-to-noise ratio (SNR).
PET and TOF-PET detectors are usually based on scintillation crystals that convert 511-keV photons

into visible light, and photosensors, which convert visible light into an electronic signal.
Regarding the configurations of PET detectors, two main geometry are used: segmented scintillators are composed of multiple crystals with a 1:1 coupling with the underlying photodetectors, position is associated with the responding photodetector; in the case of monolithic scintillators, a single block of crystal is used, an interaction event can be detected by more than one photodetector, but each of them responds with different intensity based on the relative position with the interaction event.
This research focuses on monolithic scintillators. These have some advantages over the segmented ones, where spatial resolution (that coincides with the crystal size) is limited by the size of the photodetector. The drawback for monolithic scintillators is that they typically require robust and optimized algorithms capable of mapping scintillation coordinates with the distribution of light on the photodetectors. The positioning algorithms can be categorized into two types: theoretical methods and machine learning methods. The disadvantage of the theoretical methods (e.g. non-linear analytical models) is their complicated calculations. On the other hand, machine learning algorithms such as k-nearest neighbor (k-NN), gradient tree boosting (GTB) or ANNs are getting more and more interest. Concerning TOF-PET detectors, temporal information is usually directly derived by the SiPM's readout electronic, however, machine learning algorithms can be implemented to reduce the temporal uncertainty. This research implements two ANNs for a monolithic detector, different studies have already pointed out the ability of ANN to effectively associate distributions with each other since it is a universal function approximator. Table 1 illustrates results from researches on position estimation with ANN for PET. The performance of the reported ANNs is evaluated as the average between the spatial FWHM along x- and y-axis given by the distribution of predicted coordinates. It is interesting to note that the related studies largely utilized smaller monolithic detectors compared to the one used in this article (50.8x50.8x20 mm^3).

	Crystal size [mm^3]	Number of nodes in hidden layers[2]	Average x,y spatial FWHM [mm]
F. Hashimoto et al. (2019)[1][1]	40×40×10	256-256-256	1.59
P. Conde et al. (2016) [2]	32.6×32.6×10	9-9	1.7
M. Wedrowski (2010) [3]	20×20×10	5-5	2
P. Bruyndonckx et al. (2008) [4]	20×10×10	5-5	1.6

[1] Data were collected by using simulation toolkits. [2] Each number refers to one layer, input and output layers are not included.

Table 1: *Comparison of research on ANNs for monolithic PET detectors positioning [5].*

In nearly all TOF-PET detectors, the time-of-interaction is estimated using simple linear methods that measure the time at which the photodetector signal crosses a predefined threshold. However, these methods don't use all the potentially useful timing information contained in the detector waveforms. Machine learning algorithms have been used to overcome this limitation, a common method consists in digitizing the rising edge of the signals and extracting features from it. A successful technique was proven by Berg et al. [6]. They used two LYSO–PMT detectors in coincidence in order to extract two digitized waveforms, which are stored as a 2D vector; this is subsequently fed into a Convolutional Neural Network (CNN) which is a class of ANN. The results demonstrate that CNN-based TOF estimation improves timing resolution by 20% compared to leading edge discrimination (231 ps versus 185 ps), and 23% compared to constant fraction discriminator (242 ps versus 185 ps).

2. Objective of the research

The main objective of this research is the idealization of two ANNs, one for PET positioning, the other for TOF-PET timing. The geometry of the detector under consideration consists of a monolithic crystal of dimensions 50.8x50.8x20 mm^3 coupled to an 8x8 matrix of SiPMs.
Figure 1 shows a schematic representation of the workflow. All data are obtained from simulations performed on the ANTS2 program. From the simulations, the response values of the SiPMs in terms of scintillation photons counts (proportional to the charge produced) are extrapolated, along with the temporal information of each SiPM. The integrated count values are used to train a dedicated positional PET ANN, which provides the two-dimensional position of the scintillation event. These coordinates are later used together with the temporal information to train a second ANN for TOF-PET timing, which outputs a correction value to reduce the temporal uncertainty.

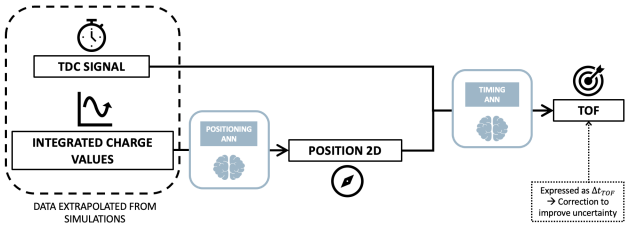

Figure 1: Schematic rapresentation of data workflow.

The purpose of the positioning ANN is basically to fit the function that maps the scintillation light distribution to the position-of-interaction. As seen in Section 1 several attempts similar to this one have been done, but very few researches were performed

on such a thick crystal. The timing ANN purpose is to elaborate the temporal information distributed among all SiPMs together with spatial information in order to improve time resolution. The main idea supporting this method is that the spatial distribution of temporal information given by the SiPM matrix constitutes a feature that an algorithm such as ANN can exploit to correct the temporal uncertainty; in other words, TOF values are not simply obtained from the first SiPM that respond, but the event temporal dynamic is exploited to provide better TOF measurements. This research is set up in such a way that it is then repeatable experimentally, moreover different methods to obtain the training datasets and two different crystals were tested.

3. Materials and methods

ANTS2 is a simulation and data processing package developed for position sensitive detectors with Anger camera type readout. The module is capable of performing particle tracking, tracing optical photons and generating photosensor signals [7]. The package also includes a time-resolved mode that provides data referred to single time bins.
The photodetectors used in this research are the silicon photomultipliers, specifically the NUV-HD FBK SiPM. The SiPMs are placed in a 8x8 matrix disposition, with a distance of 6.4 mm center to center, hence forming a 51x51 mm^2 array. A 1 mm layer of Optical Grease BC-630 from Saint-Gobain is placed above the SiPM matrix; the optical grease is a transparent, colorless, silicone-based optical coupling compound used to facilitate coupling between SiPMs and scintillation crystals. Two crystals and three different configuration are evaluated:

1. **$LaBr_3$(Ce) + Teflon**: a Cerium-doped Lanthanum(III) Bromide crystal is coated with a 1 mm layer of Teflon. $LaBr_3$(Ce) is incorporeted in a 1 mm layer of glass since this crystal is hygroscopic (meaning that exposition to air umidity affects the crystal). Scintillation crystals are usually externally wrapped with reflective materials such as Teflon, in order to convey all scintillation photons towards the photodetectors.
2. **LYSO(Ce) + Teflon**: a Cerium-doped Lutetium Yttrium Orthosilicate crystal is coated with a 1 mm layer of Teflon. The glass coating is not present since LYSO is not a hygroscopic material.
3. **LYSO(Ce) + ESR**: same crystal as point 2 but the coating material is changed to an enhanced specular reflector (ESR) [8], which is an ultra-high reflectivity, mirror-like optical enhancement film.

The main difference between Teflon and ESR is in the light reflection mode: Teflon absorbs 2% of light and scatters back 98% of light following a 180° Lambertian distribution; ESR absorbs 2% of light and the remaining 98% is specularly reflected back.
The gamma source is modeled by a cylindrical volume of 5 mm height and 1 mm diameter, output photons have an energy of 511 keV and they are collimated in order to form a pencil beam perpendicularly entering the crystal surface. The data needed to build training and test datasets were collected by translating the source along the x-y plane (see Figure 2 for the reference system), following a grid of points, at each point 500 events were recorded.

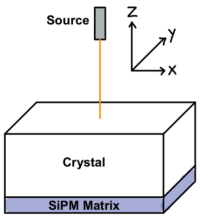

Figure 2: *Detector geometry recreated in the simulation environment, center of the reference system is located at the center of the crystal.*

Three datasets were collected corresponding to three different grid configurations:

- grid 51x51: composed by 51x51 points, 1 mm spacing between points, grid vertices are at coordinates (±25,±25)
- grid 50x50: composed by 50x50 points, 1 mm spacing between points, grid vertices are at coordinates (±24.5,±24.5)
- grid 11x11: composed by 11x11 points, 5 mm spacing between points, grid vertices are at coordinates (±25,±25)

The main steps in preparing the dataset for the positioning ANN are as following:

- Data are filtered based on the total counts detected by the SiPM matrix, in order to discard events during which the gamma photon did not fully interact with the crystal. Filtering is performed by fitting the total counts' histogram with a gaussian function, data outside the interval $[mean - FWHM, mean + FWHM]$ are discarded (see Figure 3).
- A realistic interaction position is computed: the signal detected by the SiPMs based on their location is better represented by the energy-weighted position of interaction $p_w = \frac{\sum_i \mathbf{x_i} \cdot E_i}{\sum_i E_i}$, where $\mathbf{x_i}$ is the vector of coordinates of the i_{th} interaction and E_i is its delivered energy.
- Each event provides 64 signals coming from the 8x8 SiPM matrix, this number is reduced to 16 values by summing signals along each row and each column; this operation preserves the positional information and it reduces the number of input values to the ANN.
- Data are normalized over the highest value present in the dataset: this is a common proce-

dure for preparing a training dataset for ANNs.
- 30% of total data is used as test dataset, the 80% of remaining data is used as training dataset, the remaining is used as validation dataset.

Regarding the temporal analysis and the timing ANN training, only grid 11x11 was used, and only $LaBr_3$(Ce) + Teflon and LYSO(Ce) + Teflon configurations were tested. A temporal coincidence experiment was modeled to train the network, and data from ANTS2 were processed precisely to simulate this setup.

ANTS2 data starts from the scintillation instant of the event, no information from source emission to scintillation instant is recorded. The 20 ns length of the simulation was divided into 200 time bins, obtaining a time resolution of 0.1 ns. Every event was assigned 64 timestamps, coming from the crossing of a threshold by the integrated time response of each SiPM; the response of a SiPM is the number of counts of scintillation photons as a function of time. Some events can present missing values for one or more timestamps, this occurs because, after a scintillation, not all SiPMs have a sufficient response to pass the threshold to get the timestamp; this phenomenon will be referred to as *under-threshold*. The problem is that the ANN's input layer expects always the same number of input values for each instance that has to evaluate. In order to overcome this problem, each under-threshold is assigned the value of the maximum timestamp recorded during that event, in this way the temporal distribution is partially preserved.

A real experiment is simulated: a reference detector is placed coincident with the test detector, the gamma source is placed in between, at distances of 5 mm and 35 mm respectively. Reference data are simulated using a Gaussian distribution with chosen mean and FWHM, parameters are inspired by a 3x3x5 mm^3 LSO(Ce) detector with a ∼89 ps time resolution [9]. Subsequentially, data from simulations, which refers to the ones provided by the test detector, are temporally shifted to include the time delay due to the gamma photon traveling from the source to the scintillation point. The data obtained so far are the time measurement t_2 of the test detector and that of the reference detector t_1. Both values represent the time between annihilation and the crossing of the threshold by the signal of the first responding SiPM. This quantity will generally be referred to as TOF. Both t_1 and t_2 refer to the exact annihilation instant, which is something that can not be retrieved experimentally. The time data that would be obtained from this experimental setup would be the value of the test detector measurement in reference to that of the reference detector. For this reason the difference between t_2 and t_1 is computed to obtain ΔTOF. Note that each coincidence event is associated with a ΔTOF, since each event from the test detector was randomly matched with an event from the reference detector, in order to simulate a coincidence event.

As already mentioned, if the detector was perfect and not subject to temporal uncertainty, the TOF distribution would be centered in a single value. In reality, the temporal uncertainty increases the width of the distribution. In order to improve TOF measurements, we want the timing ANN to learn the correction needed to tighten the distribution and to reduce uncertainty, hence the difference between the recorded TOF and the mean value between all TOFs. This quantity will be called *correction* Δt and provides the label to be assigned to the i_{th} event, calculated through the following formula:

$$\Delta t_i = \Delta TOF_i - \frac{\sum_j^N \Delta TOF_j}{N}$$

where N is the total number of events used for training the timing ANN.

When dealing with experimental data, timestamps values are affected by photon time travel, distance between detectors, and measurement global clock. To get a performing method regardless of where the data is centered, we need to train the network with data that is not dependent on these factors but easily retrievable to be given to the network during TOF-PET imaging, regardless of all the conditions that may vary between measurements. If all timestamps are subtracted from the minimum of timestamps (i.e. the TOF) for that event, the delay between the first and other timestamps is obtained. These values preserve the temporal dynamic that the ANN must use to retrieve the correction, meanwhile, they are not referred to any offset.

4. Results

4.1. Data analysis

Before implementing the network, some properties of the collected data were analyzed, in order to understand the characteristics of the scintillation photons and how SiPMs respond to them.

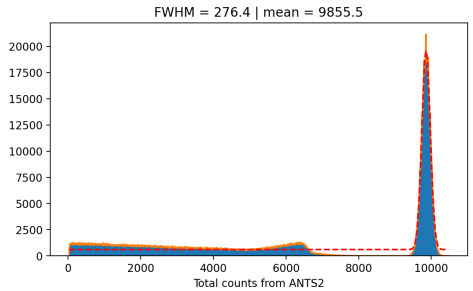

Figure 3: *Total counts histogram fitted with a Gaussian function. $LaBr_3$(Ce) + Teflon configuration.*

Figure 3 shows the distribution of the total counts detected from the SiPM matrix, this variable is

directly related to the total energy detected, in fact, it is the parameter with which experimentally the data are usually filtered. The events that form the Gaussian peak are those that almost totally delivered the 511 keV of the gamma photon. These are the ones retained after filtering and they account for 48.7% of the original data.
Figure 4 represents the distribution of ΔTOF values coming from the simulated coincidence experiment (procedure explained in Section 3). The delay due to the distance between the source and the scintillation point has already been added.

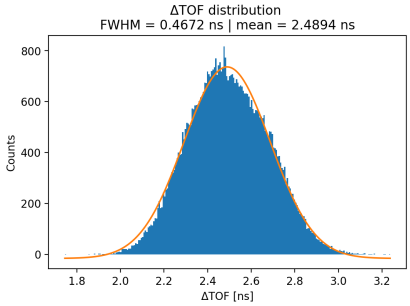

Figure 4: *ΔTOF distribution.*

Figure 5 presents a study on the variability of the timestamps given by a single event, in function of its TOF. Standard deviation was used to quantify the variability of each sample. The data were partitioned according to the TOF of the event, dividing the distribution into 11 classes.

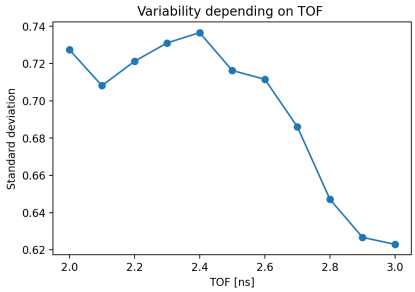

Figure 5: *TOF-dependent variability.*

Figure 6 is intended again to demonstrate the concept expressed in the previous paragraph: the distribution of timestamps is related to the relative TOF, the two figures shows that as TOF increases, the distribution of timestamps tightens. The figure is correlated by two drawings showing where the variability in timestamps comes from: when scintillation occurs close to the photodetectors, photons arrive at relatively very different times on the SiPMs (Figure 6a), in contrast, arrival times are very similar for scintillations with high TOF and low DOI (Figure 6b).

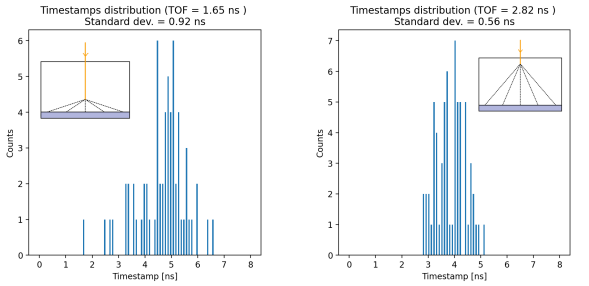

(a) *Event with high timestamps variability and low TOF.*

(b) *Event with low timestamps variability and high TOF.*

Figure 6

The Δt corrections needed for the two events in Figure 6 are respectively -0.557 ns and 0.603 ns. It is from this that one can infer that the sign and absolute value of the correction are related to the temporal distribution of timestamps. This relationship is the one that the timing ANN should model. The addition of the two-dimensional interaction coordinates should help the network recognize particular effects due to proximity to detector edges.

4.2. ANNs results

Figure 7 shows the trend of the loss function during the training process, for both training and validation sets. Values are plotted in function of the epoch. A very similar graph is obtained also for the positioning ANN.

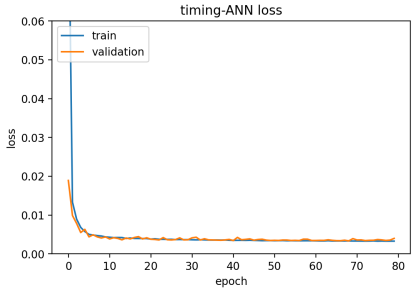

Figure 7: *Learning curve of the timing ANN. $LaBr_3(Ce)$ + Teflon | 11x11 grid.*

Two main figures of merit are used to present results on positioning ANN:

- *Spatial error* is the euclidian distance between the given label (coordinates of source position) and the predicted coordinates. It expresses the magnitude of the error made by the network.
- *Spatial FWHM* is given by a Gaussian fitting applied on the spatial distribution of the predicted coordinates, around the entry point. It is computed for both x- and y- axes, and the average value of the two is reported. FWHM is related to the spatial resolution of the detected image.

Several ANN networks were tested, the best performances were obtained by structures with hidden layers composed of a number of nodes equal to powers of 2. In particular, 256-256 structure for $LaBr_3(Ce)$ and the 256-256-128-64 structure for LYSO(Ce) seem to perform slightly better for the two crystals. All investigated networks use the ReLu activation function for the nodes in the hidden layers; a linear activation function is always used in the output layer since these ANNs perform a regression. The chosen loss function is the mean squared error.
Regarding the positioning part, each scintillator configuration was trained with both grid 51x51 and grid 11x11. Only $LaBr_3(Ce)$ + Teflon was also trained with the combination of 51x51 grid + 50x50 grid in order to understand how an increased resolution of the training dataset affects the positioning ANN's performance.

Grid	mean spatial error [mm]	mean spatial FWHM [mm]
51x51	1.807	2.107
51x51 + 50x50	1.704	2.074

Table 2: *Training grid comparison using $LaBr_3(Ce)$ + Teflon.*

Figure 8 represents the magnitude of the spatial FWHM based on the position along the x-y plane; each 1x1 mm^2 square refers to the spatial distribution around each point of the test grid.

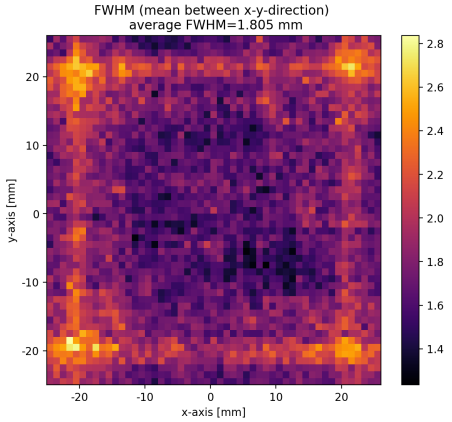

Figure 8: *Spatial FWHM. LYSO(Ce) + ESR | 51x51 grid.*

Table 3 shows the average values of the two figures of merit over all the area, for the 6 different combinations of configurations under consideration.

Configuration	51x51 grid		11x11 grid	
	mean spatial error [mm]	mean spatial FWHM [mm]	mean spatial error [mm]	mean spatial FWHM [mm]
$LaBr_3(Ce)$ + Teflon	1.807	2.107	2.216	2.578
LYSO(Ce) + Teflon	1.538	2.195	2.271	2.342
LYSO(Ce) + ESR	1.226	1.805	1.612	2.368

Table 3: *Positioning ANNs results comparison.*

Figure 9 is an attempt to show how the positioning ANNs predict a given image, it consists of a 2D histogram of predicted coordinates from the 11x11 grid, darker spots contain more counts.

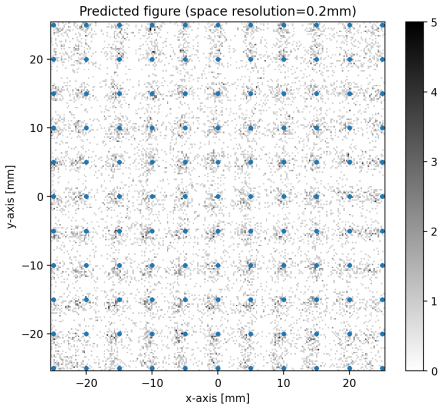

Figure 9: *Prediction of the 11x11 grid (blue points). Greyscale represent the count of predicted points in a 0.2x0.2 mm^2 square.*
LYSO(Ce) + ESR | 51x51 grid

Figure 10 is nothing more than the distribution of the corrected ΔTOFs, computed using:

$$\Delta TOF_{corrected} = \Delta TOF - \Delta t_{predicted}$$

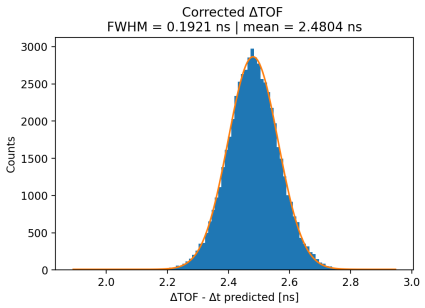

Figure 10: *Corrected ΔTOFs distibution.*

The *Improvement* (I) was used to quantify the timing ANN performance, it is defined as:

$$I = \frac{FWHM_{original}}{FWHM_{corrected}} \cdot 100\%$$

where $FWHM_{original}$ refers to the original ΔTOF distribution, and $FWHM_{corrected}$ refers to the cor-

rected ΔTOF distribution.
The timing ANN structure that best corrects the ΔTOF distribution for every configuration consists of two hidden layers, made of 64 and 32 nodes respectively.
Table 4 shows the results for the two configurations, each with thresholds set at 1 and 3 photons.

	$LaBr_3$(Ce) + Teflon		LYSO(Ce) + Teflon	
	Threshold = 1 phe	Threshold = 3 phe	Threshold = 1 phe	Threshold = 3 phe
$FWHM_{original}$ [ps]	282	467	340	561
$FWHM_{corrected}$ [ps]	189	192	246	272
Improvement	149%	243%	138%	206%

Table 4: *Timing ANN results for different setups and thresholds.*

5. Discussion

The fitting results shown in Figure 7 demonstrate a good fitting of the ANN over the training dataset. Both training and validation plots decrease to a point of stability with a minimal gap between the two final loss values, proving that the training data is representative of the problem. The curves flatten out toward the end of the graphs, suggesting that more epochs would not significantly improve performance.
Table 2 shows that there is a relatively small improvement when the spatial resolution of the training dataset is increased. The improvement is not so high to justify the large increase in calibration time that one would have to use to collect 51x51+50x50 points instead of 51x51 points.
From Figure 8 the spatial dependency of ANN performances is evident. The spatial resolution is best at the center of the crystal and starts to degrade toward the edges. It is interesting to note that the spatial FWHM gets worse in an intermediate region, at about 5-7 mm far from each edge. This effect is due to the reflection of scintillation light at the sides of the crystal, which affects the light distributions on the SiPM matrix making it increasingly similar for nearby interaction positions toward the detector edges. Thus, the ability of the ANN to predict the correct position generally deteriorated by nearly 50% among all configurations.
The results shown in Table 3 are in line with previous research on such thick crystals, as expected performances are better when the training spatial resolution is higher, however it should be considered that a considerable reduction in training points corresponds to a relatively small worsening. The best configuration is the LYSO(Ce) + ESR; LYSO(Ce) performs generally better than $LaBr_3$(Ce), and the mean spatial error is the one that benefits most from the transition from Teflon to ESR. There is to consider that the results on spatial FWHM are affected by two factors: the source pencil beam diameter of 1 mm, and the Compton scattering, since the gamma photon can be deviated and can deliver its energy in secondary interactions, resulting in a p_w coordinate different from the entering x-y position. In fact, the average spatial FWHM of the p_w distribution over the crystal surface is 0.446 mm for LYSO(Ce) + Teflon.
Finally, the consequences of the spatial FWHM can be better appreciated in Figure 9, which is a visualization of the detector 2D point spread function (PSF), directly related to how the detector detects point figures, in this case, the 11x11 grid.
Results presented in Figure 10 are promising. The distribution of the corrected ΔTOF has a FWHM of 192.1 ps, against the one of the original ΔTOF which is 467.2 ps, meaning that temporal data uncertainty is corrected considerably. It should not be forgotten that the data presented are distributions, which means that among the adjusted ΔTOFs there are still events for which the temporal uncertainty deviates them from the mean (those toward the tails of the distribution), but the magnitude of this effect is much smaller than for the unadjusted ΔTOFs; this means that the probability of finding different time measurements from each other (for same detector and the same distance from the source) is reduced when the timing ANN is used.
It can be demonstrated that the corrected ΔTOF distribution (Figure 10) coincides with the error made by the network in predicting the Δt, except for a constant:

$$\Delta t - \Delta t_{pred.} = \Delta TOF - \frac{\sum_j^N \Delta TOF_j}{N} - \Delta t_{pred.} = \\ = \Delta TOF_{corrected} - \frac{\sum_j^N \Delta TOF_j}{N}$$

Since the mean $\frac{\sum_j^N \Delta TOF_j}{N}$ is a constant value, the equation shows that the uncertainty of the network in making the prediction is directly reflected in the uncertainty of the final outcome. Hence, by improving the timing ANN's capability of prediction, temporal uncertainty is directly reduced. It is to note that, the results obtained depend only on the FWHM of the ΔTOF distribution, which is an intrinsic property of the test detector (partly conditioned by that of the reference detector used during training), results do not depend on where the distribution is centered; this means that the proper correction is applied even if the time data have different delays due to sources at different distances, as happens during TOF-PET imaging, since the spatial delay is only a constant. Once the network is trained on a particular detector, it is ready to correct TOFs unless the intrinsic variability worsens, e.g. due to factors such as environmental influences on photodetectors or electronics; it would be interesting to study this

dependence through the experimental application of this research.
With regard to the data presented in Table 4, it can be seen that the configuration $LaBr_3$(Ce) + Teflon generally gives better results, this is not surprising given that $LaBr_3$(Ce) has a faster response due to its short decay time, together with a higher light yield which improves the SiPMs response. The 1 photon threshold gives better results than the 3 photons one, but the ANN has a greater improvement on the latter. This could be due to the greater variability of the integrated responses of SiPMs as they develop over time. It is noteworthy that the integrated response and not the instantaneous response was chosen precisely to emphasize the slope of the response with its intensity, thus its closeness to scintillation. However, the choice of threshold must be made considering the noise of the readout electronic in use (state of art electronics are able to detect a single photon and even less).

6. Conclusions

The current thesis work aimed to provide a new method to exploit ANN's capabilities for the benefit of PET and TOF-PET imaging systems. The research focuses on two main objectives: using a positioning ANN to predict the scintillation position and a timing ANN to improve the detector time resolution.
Through simulations, it was possible to train a positioning ANN with good spatial resolution on relatively thick crystals. Results for different configurations were compared, such as different training datasets, different crystals, and coatings; the best setup showed a 1.805 mm spatial FWHM.
The second part showed that is possible to correct temporal information by giving the timing ANN all timestamps collected by a SiPM matrix. The time delay between timestamps appears to be the information capable of making the proper correction to the detector's inherent temporal uncertainty. For the setup on which the network performs best, we went from a TOF uncertainty of 467 ps FWHM to one of 192 ps FWHM.
Future development can aim to improve the ANN's performances, by testing new structures or using different hyperparameters. Regarding the setup, it would be interesting to extend the variability of the training datasets by using events incident to the crystal at an angle other than 90 degrees. As well as exploiting crystals with instantaneous scintillation, such as the ones that emit Cherenkov photons. Finally, increasing the simulation time resolution could lead to better performances of the timing ANN since the timestamp variability could be better appreciated.

References

[1] Fumio Hashimoto, Kibo Ote, Ryosuke Ota, and Tomoyuki Hasegawa. A feasibility study on 3d interaction position estimation using deep neural network in cherenkov-based detector: A monte carlo simulation study. *Biomedical Physics & Engineering Express*, 5(3):035001, 2019.

[2] P Conde, A Iborra, AJ González, L Hernández, P Bellido, L Moliner, JP Rigla, MJ Rodríguez-Álvarez, F Sánchez, M Seimetz, et al. Determination of the interaction position of gamma photons in monolithic scintillators using neural network fitting. *IEEE Transactions on Nuclear Science*, 63(1):30–36, 2016.

[3] Mateusz Wędrowski. *Artificial neural network based position estimation in positron emission tomography*. PhD thesis, Ph. D. dissertation, Vrije Universiteit Brussel, 2010.

[4] Peter Bruyndonckx, Cedric Lemaitre, DJ Van Der Laan, Marnix Maas, Dennis Schaart, Wang Yonggang, Zhi Li, M Krieguer, and Stefaan Tavernier. Evaluation of machine learning algorithms for localization of photons in undivided scintillator blocks for pet detectors. *IEEE Transactions on Nuclear Science*, 55(3):918–924, 2008.

[5] Ting-Yi Yang. Machine learning for high resolution 3d positioning of. 2019.

[6] Eric Berg and Simon R Cherry. Using convolutional neural networks to estimate time-of-flight from pet detector waveforms. *Physics in Medicine & Biology*, 63(2):02LT01, 2018.

[7] Andrey Morozov, V Solovov, R Martins, F Neves, V Domingos, and V Chepel. Ants2 package: simulation and experimental data processing for anger camera type detectors. *Journal of Instrumentation*, 11(04):P04022, 2016.

[8] Vikuiti™ enhanced specular reflector (esr) (website). `https://lphe.epfl.ch/bay/www/scifimats/matprod/Materials/ESR_Usage_Guidelines.pdf`. Accessed: 2022-05-24.

[9] Giacomo Borghi, Valerio Tabacchini, Stefan Seifert, and Dennis R Schaart. Experimental validation of an efficient fan-beam calibration procedure for k-nearest neighbor position estimation in monolithic scintillator detectors. *IEEE Transactions on Nuclear Science*, 62(1):57–67, 2015.